

Template bank to search for exotic gravitational wave signals from astrophysical compact binaries

ABHISHEK SHARMA^{1,*}, SOUMEN ROY^{2,3,†} and ANAND S. SENGUPTA^{1,‡}

¹*Indian Institute of Technology Gandhinagar, Gujarat 382055, India.*

²*Nikhef, Science Park 105, 1098 XG Amsterdam, The Netherlands.*

³*Institute for Gravitational and Subatomic Physics (GRASP), Utrecht University, Princetonplein 1, 3584 CC Utrecht, The Netherlands.*

Modeled searches of gravitational wave signals from compact binary mergers rely on template waveforms determined by the theory of general relativity (GR). Once a signal is detected, one generally performs the model agnostic test of GR, either looking for consistency between the GR waveform and data or introducing phenomenological deviations to detect the departure from GR. The non-trivial presence of beyond-GR physics can alter the waveform and could be missed by the GR template-based searches. A recent study [1] targeted the binary black hole merger, assuming the parametrized deviation in lower post-Newtonian terms and demonstrated a mild effect on the search sensitivity. Surprisingly, for the search space of binary neutron star (BNS) systems where component masses range from 1 to 2.4 M_{\odot} and parametrized deviations span 1σ width of the deviation parameters measured from the GW170817 event, the GR template bank is highly ineffectual for detecting the non-GR signals. Here, we present a new hybrid method to construct a non-GR template bank for the BNS search space. The hybrid method uses the geometric approach of three-dimensional lattice placement to cover most of the parameter space volume, followed by the random method to cover the boundary regions of parameter space. We find that the non-GR bank size is ~ 15 times larger than the conventional GR bank and is effectual towards detecting non-GR signals in the target search space.

I. INTRODUCTION

With the advent of terrestrial observatories such as Advanced LIGO [2], Advanced Virgo [3] and KAGRA [4], the gravitational waves (GWs) from compact binary coalescences (CBCs) [5–7] allow us to conduct tests of General Relativity (GR) [8–12]. In addition to GWs, GR has also been tested using solar system observations [13], binary pulsar observations [14–16], and observations of supermassive black holes (BHs) at the center of galaxies [17–19]. None of them have found any statistically significant deviation yet, which concludes that GR is the most accurate theory of gravity known to date. In particular, compact binary mergers can probe gravity at its most extreme environment characterized by highly dynamical, non-linear and genuinely strong-field regime. Therefore, such systems are exceptional laboratories for unravelling the beyond-GR physics.

The observations and tests of beyond-GR physics with CBCs can be designed by availing the accurately modeled waveforms for beyond-GR theories. Unfortunately, one lacks a complete understanding of the dynamics of coalescing compact binary in the strong-field regime, in nearly all alternative theories of gravity. Recently, there has been progress toward numerical relativity (NR) simulations of binary black hole mergers in theories beyond

GR [20–22]. Some of these simulations approximately solve the underlying field equations. In addition to some early developments in NR front, several efforts have been made obtaining the analytical gravitational waveforms in alternative theories [23–27]. However, a lot more work is still required before these early developments can be incorporated in GW data analysis. Moreover, there might be a more accurate alternative theory, which is unknown to us. Thereby, we generally perform model agnostic analyses: looking for consistency between GR waveform and data [28–32], introducing phenomenological deviations to detect the departure from GR [33–36]. One example of latter kind of analysis is the *parametrized test* of GR, where one measures the deviations in various post-Newtonian (PN) terms of the GR predicted waveform phase.

All these tests are performed after a GW signal is detected by one of the several search pipelines. The search techniques can be broadly divided into two categories: generic transient searches and template-based searches. The first kind, such as cWB [37, 38] and oLIB [39, 40], uses minimal assumptions on the GW signature, but are inefficient for long duration signals or when the signal-to-noise ratio (SNR) is low. On the other hand, the template-based searches such as GstLAL [41, 42], MBTA [43], PyCBC [44–46] and SPIIR [47], completely rely on the GR template waveform and are highly efficient for long duration signals. However, a gravitational wave signal carrying a significant amount of non-GR physical effects (in terms of non-zero deviation in the GR-predicted PN phasing coefficient(s)), could be missed by the GR template-based search pipelines.

* sharma.abhishek@iitgn.ac.in

† soumen.roy@nikhef.nl

‡ asengupta@iitgn.ac.in

A recent study [1] demonstrated a method for a *bottom-up* search for the GW signals that may carry deviations in the PN phasing coefficients from the template waveforms predicted by GR. The study highlighted that the GR bank would fail to detect such a non-GR signal and further showed an improvement in sensitivity for detecting non-GR signals when searched using a non-GR template bank. The study focused on the stellar mass BBH systems ($m_{1,2} \in [5, 50] M_{\odot}$). The parametrized deviations were considered only in the lower PN terms (upto 2PN) over a range spanning the 90% credible interval of the posterior distribution reported in the test of GR using events in the GWTC-1 [10]. The fitting factor¹ study of GR template bank for non-GR injections revealed that 20% injections were recovered below the bank’s minimal match of 0.97. In this paper, we target the binary neutron star (BNS) systems ($m_{1,2} \in [1, 2.4] M_{\odot}$) with LIGO’s O2 sensitivity², consider fractional deviations in all eight PN terms of the waveform phase (restricted upto 3.5PN) and over a range spanning the 1σ (68%) credible interval of the posterior distribution reported in the test of GR for GW170817 [9]. Surprisingly, the fitting factor study indicates that the GR template bank for BNS search space is highly ineffectual for detecting the non-GR signals, as shown in Figure 1. Suppose a GW signal from a BNS-like system carries non-GR effect. In that case, it is likely to be missed by the template-based search pipelines and also the unmodeled search pipelines due to their inefficiency for long-duration signals. Note that the conventional parametrized test conducted by LVK collaboration considers varying single PN deviation parameter at a time since searching for a departure from GR assuming multi-parameter deviation leads to an uninformative posterior [8, 36, 48]. However, in a modified theory of gravity, one might expect modifications in more than one PN coefficients. That’s why we allow to vary all the PN coefficients to define our non-GR search space.

We present a hybrid method for placing non-GR templates in the search space of BNS-like systems, which is adequate to cover the possible non-GR space in terms of the parametrized deviation of the PN phasing coefficients. Following [49], we first construct a metric on the parameter space of TaylorF2 coefficients and identify that the effective dimension is three, albeit the non-GR search space is twelve dimensional. We then place the template points using the \mathcal{A}_3^* lattice for most of the parameter space volume. Since the boundaries in the effective three dimensional non-GR parameter space are unknown, we use the top-down part of the hybrid-geometric random

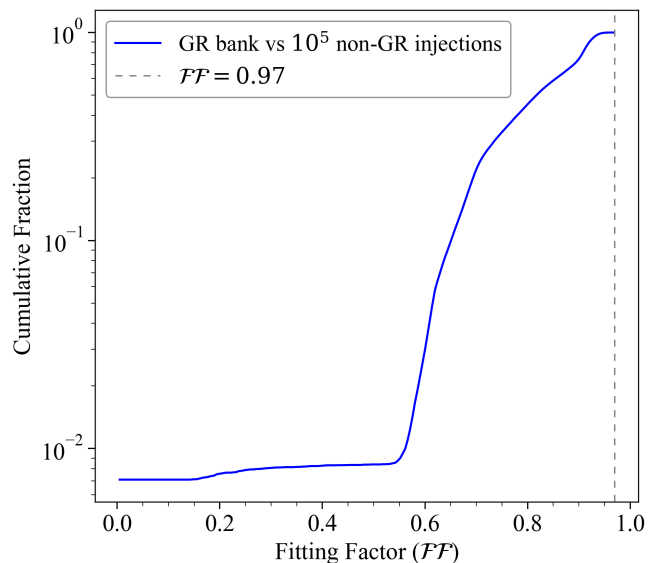


FIG. 1. Cumulative distribution of the fitting factor of GR template bank for 10^5 non-GR signal waveforms computed for LIGO’s O2 sensitivity curve. The GR template bank for BNS search space is generated assuming the mass-spin parameter ranges given in the first two rows of Table I, and the minimal match is set to be 0.97. The ranges of the deviation parameters for generating the non-GR signals are given in the same Table. None of the injections is found above the desired fitting factor value of 0.97, and 709 injections have zero fitting factor for which the curve ended at ~ 0.007 instead of 10^{-5} . The details of the template bank generation and fitting factor studies are described in Section III and Section IV, respectively.

template placement method [50] to cover the entire parameter space. Further, we notice that the metric approximation overestimates the match when the deviation parameters are non-zero. Therefore, we build the final hybrid bank using the exact match function.

The rest of this paper is organized as follows: in Section II, we motivate and describe the search parameter space and the choice of waveform model used to construct the template bank; in Section III, we describe in detail the method used to construct the template bank to search for exotic gravitational wave signals; in Section IV, we demonstrate the results of validation studies performed to quantify the effectualness of the template banks. Finally, we summarize, conclude and discuss possible future directions in Section V.

II. WAVEFORM MODEL AND SEARCH PARAMETER SPACE

Neutron stars are formed from the collapse of much heavier stars and in order to conserve angular momentum during collapse, the neutron stars are bound to have large spin at their birth. However, the spinning rate decreases with time due to the magnetic drain of their energy. It

¹ The fitting factor of a template bank for an arbitrary signal is defined as the maximum value of match over all the templates, given in Equation (8).

² Average multi-detector noise PSD: the harmonic mean of the power spectral densities measured from the Hanford and Livingston detectors <https://github.com/gwastro/pycbc-config/tree/65138ade78b234a805e49b694db1c17c20948ecc/D2/psd>

is expected to decay away long before entering the band of interest for ground-based gravitational wave observatories [51]. Consequently, previous studies found that aligned spin template waveforms are sufficient for detecting generic spinning BNS systems with second-generation detectors [49]. As the post-inspiral and merger signal is emitted at very high frequencies where the second-generation detectors are less sensitive, the signal-to-noise ratio is dominated by the inspiral signal. Therefore, we only consider the inspiral of the two bodies in this work. The inspiral phase of the waveform can be modeled analytically using the PN framework [52]. The waveform in the frequency domain can be expressed as,

$$\tilde{h}(f) = \mathcal{A}(f; D_L, \hat{n}, \vec{\lambda}) \exp \left\{ -i\Psi(f; t_c, \phi_c, \vec{\lambda}) \right\}, \quad (1)$$

where D_L is luminosity distance to the source, \hat{n} describes the sky location (α, δ) and polarization angle (ψ) that only affect the overall amplitude and phase of the signal, t_c is the geocentric coalescence time, ϕ_c is the coalescence phase, $\vec{\lambda}$ refers to the set of intrinsic parameters comprising component masses ($m_{1,2}$) and dimensionless spins ($\chi_{1,2}$). The waveform phase $\Psi(f)$ for TaylorF2 can be expanded as [53, 54],

$$\begin{aligned} \Psi(f) = & 2\pi f t_c - \varphi_c - \frac{\pi}{4} \\ & + \sum_{k=0}^7 \left[\varphi_k(\vec{\lambda}; f_0) + \varphi_k^\ell(\vec{\lambda}; f_0) \log x \right] x^{(k-5)/3}, \end{aligned} \quad (2)$$

where $x = f/f_0$ and f_0 is a fiducial frequency. The expansion order k corresponds to $(k/2)$ -PN term. Various coefficients at different PN orders are given in Appendix A.

All the PN phasing coefficients are uniquely determined for given values of the intrinsic parameters. Any deviation from GR would change the binding energy and angular momentum of the binary, thus, transform the equations of binary motion. Alternative theories of gravity will have different functional dependence of PN-phasing coefficients on intrinsic parameters. It has been motivated to devise a parametrized test of GR that work by introducing a fractional deviation parameter ($\delta\hat{\varphi}_i$) for each phase coefficient φ_i [33, 55–57],

$$\tilde{\varphi}_i = (1 + \delta\hat{\varphi}_i)\varphi_i^{\text{NS}} + \varphi_i^{\text{S}}, \quad (3)$$

where φ_i^{NS} and φ_i^{S} are the non-spinning and spin related terms of φ_i , respectively.

A waveform carrying a nonzero deviation parameter is referred to as a *non-GR* waveform. If a gravitational wave signal carries a significant amount of non-GR physical effects it would be missed by the GR template-based search pipelines as described in [1]. This study targeted the BBH search space and allowed deviations in four PN terms from 0.5PN to 2PN order. In this work, we consider the search space of BNS systems and all the deviation parameters up to 3.5PN order. We choose the posterior samples from the parameterized test of GW170817

event studied by LVK [9] and consider 1σ interval of the marginal posterior distribution of the deviation parameters to define the boundaries of the non-GR space. Parameter ranges for the template bank construction are tabulated in Table I.

Parameter	Limits
Component masses	$m_{1,2} \in [1, 2.4] M_\odot$
Component spins	$\chi_{1,2} \in [-0.05, +0.05]$

Deviation parameters	
0.0 PN	$\delta\hat{\varphi}_0 \in [+0.029, +0.261]$
1.0 PN	$\delta\hat{\varphi}_2 \in [-0.084, +0.001]$
1.5 PN	$\delta\hat{\varphi}_3 \in [-0.032, +0.171]$
2.0 PN	$\delta\hat{\varphi}_4 \in [+0.329, +2.387]$
2.5 PN (log-term)	$\delta\hat{\varphi}_5^\ell \in [-0.697, -0.099]$
3.0 PN	$\delta\hat{\varphi}_6 \in [+0.266, +1.715]$
3.0 PN (log-term)	$\delta\hat{\varphi}_6^\ell \in [-5.815, -0.881]$
3.5 PN	$\delta\hat{\varphi}_7 \in [-7.067, -1.269]$

TABLE I. Parameter ranges used in generating the template bank. The description of parameters below the horizontal dashed line corresponds to the 68% credible intervals of the deviation in PN coefficients obtained from the parameterized analysis on GW170817 as shown in Figure 2.

III. TEMPLATE BANK CONSTRUCTION

The long-established method for searching gravitational waves from compact binary mergers relies on the matched filter technique as it is an optimum method to detect a signal if the data contains stationary Gaussian noise. It is accomplished by performing convolution between the data and a set of theoretical filter waveforms to obtain a maximized SNR. In principle, one can maximize the SNR over time, overall amplitude, and overall phase by employing analytical tricks [59–61]. The noise free response of a LIGO-like detector is given by,

$$h(t) = F_+(\alpha, \delta, \psi) h_+(t) + F_\times(\alpha, \delta, \psi) h_\times(t), \quad (4)$$

where h_+ and h_\times are two polarizations of gravitational wave, and F_+ and F_\times are the antenna response function for the two polarizations. For dominant $(2, \pm 2)$ mode of gravitational wave signals emitted from nonprecessing binary systems, two polarizations are proportional to each other, $\tilde{h}_+ \propto i\tilde{h}_\times$, where $\tilde{h}_{+, \times}$ denotes the Fourier transform of $h_{+, \times}$. Note that this relation deviates when we include the contribution of higher harmonics or precession to the waveform. When this relation holds, the extrinsic parameters such as the sky location, inclination angle, polarization angle, coalescence phase, and distance to the source can all be expressed as overall amplitude and phase. The intrinsic parameters that can not be absorbed in the analytical maximization procedure, such

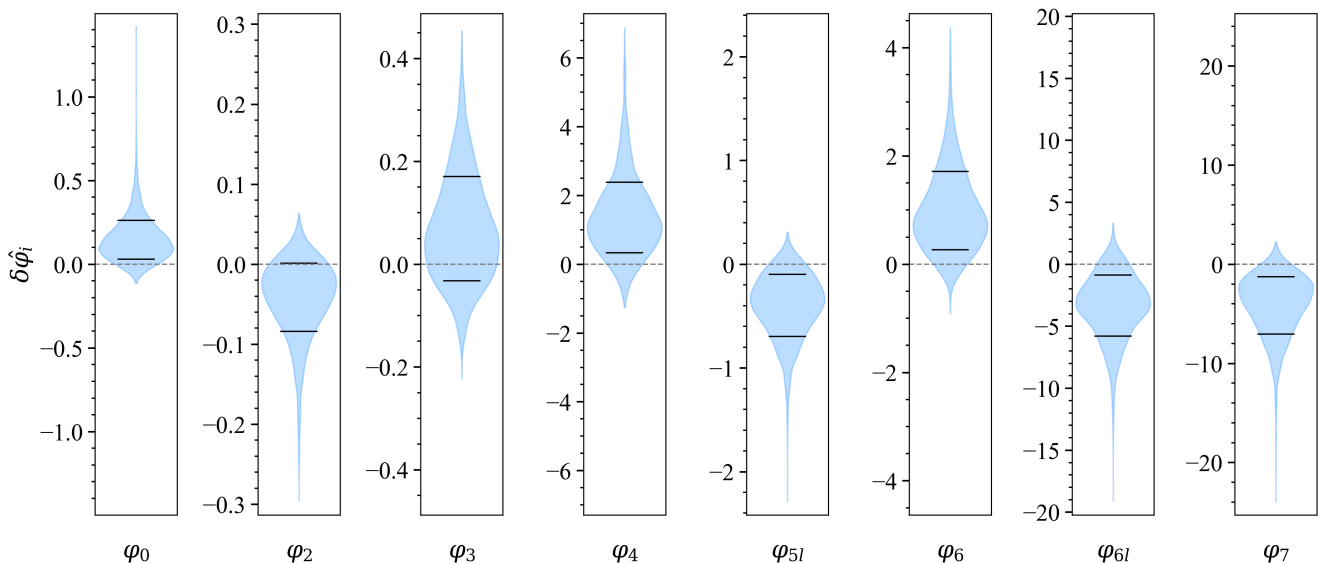


FIG. 2. Posterior distribution for deviation parameters obtained from the parameterized test with GW170817 event [58]. Black horizontal ticks mark the 68% credible interval. The grey horizontal dashed line corresponds to the GR prediction.

as component masses and component spins, must be varied to obtain the maximized SNR by generating the filter waveforms repetitively. Our chosen waveform model, TaylorF2 upholds this relation for both the GR and non-GR waveforms. Therefore, we generate the filter waveforms by varying the intrinsic parameters to obtain the optimal SNR. We evaluate the filter waveforms in the parameter space comprising of component masses and component spins for the GR case and over additional eight deviation parameters for the non-GR case. This discrete set of points in the parameter space constitutes a template bank.

When searching for a signal in data d using a template waveform h , the matched filtered SNR is computed by maximizing the inner product between d and h over an overall amplitude, phase (φ_{ref}), and time (t_{ref}),

$$\rho_{\text{MF}} = \max_{t_{\text{ref}}, \varphi_{\text{ref}}} \langle d | \hat{h} \rangle, \quad (5)$$

where \hat{h} is the normalized template waveform such that $\hat{h} = h / \sqrt{\langle h | h \rangle}$ and the inner product $\langle \cdot | \cdot \rangle$ is defined as,

$$\langle a | b \rangle = 4 \Re \int_{f_{\text{low}}}^{f_{\text{high}}} \frac{\tilde{a}^*(f) \tilde{b}(f)}{S_n(f)} df, \quad (6)$$

where $S_n(f)$ is the one-sided noise power spectral density. Suppose the template waveform does not *exactly* match the signal in the data even after maximizing over the extrinsic parameters. In that case, we will lose a fraction of SNR, which is determined by the mismatch ($1 - \mathcal{M}$) between them. The quantity \mathcal{M} denotes the match between two waveforms:

$$\mathcal{M}(a, b) = \max_{t_{\text{ref}}, \varphi_{\text{ref}}} \langle \hat{a} | \hat{b} \rangle \quad (7)$$

To quantify the effectualness of a template bank (\mathcal{T}) for detecting an arbitrary signal $h_a(t)$, we calculate the *fitting factor* (\mathcal{FF}) which is defined as maximal match between arbitrary signal and templates in the bank [62],

$$\mathcal{FF}(h_a) = \max_{\vec{\lambda} \in \mathcal{T}} \mathcal{M}(h_a, h(\vec{\lambda})), \quad (8)$$

where $\vec{\lambda}$ denotes one of the template points.

A. Parameter Space Metric

Following [63], the match between two nearby waveforms, whose intrinsic parameters are infinitesimally separated by $\Delta \vec{\lambda}$, can be Taylor expanded up to the quadratic terms about $\Delta \vec{\lambda} = 0$ which in turn, can be rearranged to express the *mismatch* ($1 - \mathcal{M}$) in terms of the parameter space metric g_{ij} as,

$$1 - \mathcal{M} \simeq g_{ij} \Delta \lambda^i \Delta \lambda^j, \quad (9)$$

where the metric is given by

$$g_{ij} := -\frac{1}{2} \left. \frac{\partial^2 \mathcal{M}}{\partial \Delta \lambda^i \partial \Delta \lambda^j} \right|_{\Delta \vec{\lambda}=0}. \quad (10)$$

An alternative approximation for computing the metric is to evaluate the Fisher information matrix of the waveforms over the full parameter space and then project out the dimensions corresponding to the extrinsic parameters [64]. The components of the Fisher information matrix are given by,

$$\Gamma_{\alpha\beta} = \left\langle \frac{\partial h(\vec{\theta})}{\partial \theta_\alpha} \middle| \frac{\partial h(\vec{\theta})}{\partial \theta_\beta} \right\rangle \quad (11)$$

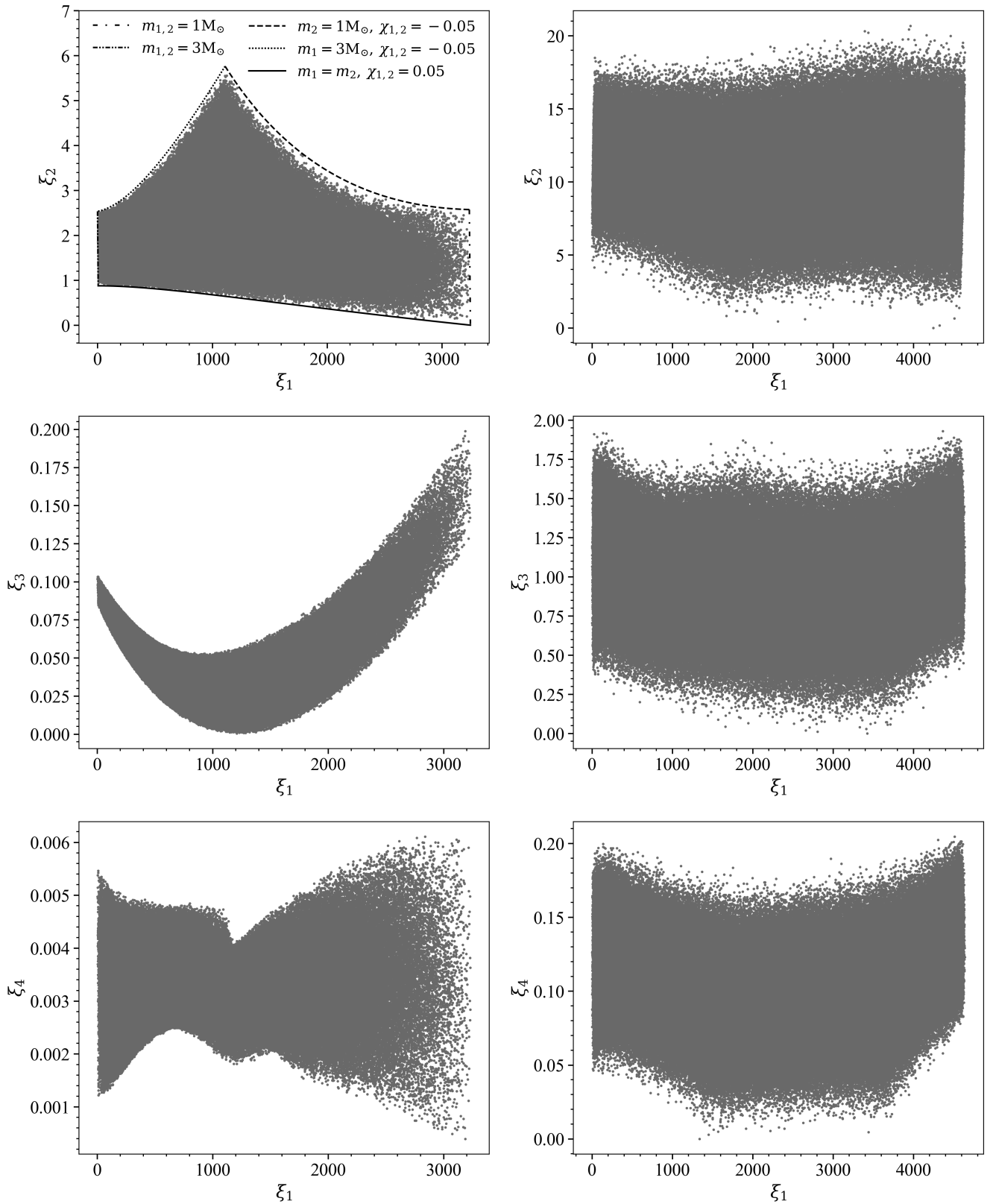


FIG. 3. The width of the parameter space along ξ_2 , ξ_3 and ξ_4 directions, plotted against ξ_1 for two distinct cases. Case I (left column): All the deviation parameters ($\delta\varphi_i$) are taken to be zero (GR-case). Case II (right column): All deviation parameters are allowed to deviate from zero and their values lie between the ranges given in Table I (non-GR case). Component masses and spins are uniformly distributed between the ranges given in Table I in both cases. Each ξ_i coordinate is scaled such that one unit corresponds to the coverage diameter of 0.97 minimal match contour, \mathcal{D}_{max} . The dashed curves in the top left plot marks the boundary of GR parameter space in $\xi_1 - \xi_2$ plane and corresponding physical parameters are given in the legend. The plot is generated using LIGO's O2 PSD with a lower cut-off frequency of 27 Hz.

where, $\vec{\theta} = \{\vec{\lambda}, \vec{\beta}\}$, such that $\vec{\lambda}$ and $\vec{\beta}$ denote the intrinsic and extrinsic parameters, respectively. The parameter space metric is a crucial input for constructing a geometric template bank in order to compute the distance between two points. When placing the templates, a suitable coordinate system is looked for in which the metric components are almost constant. Under this scheme, a coordinate system with minimum extrinsic curvature is considered good. Following [49, 65], we use the PN phasing coefficients comprising six φ_i and two logarithmic terms φ_i^ℓ given in Appendix (A) to define the coordinate system. The metric on this eight-dimensional (henceforth, written as 8-D) parameter space does not have intrinsic curvature—the metric components are constant for any point in parameter space. As described in [49, 63], we similarly use Equation (10) to first evaluate the metric on 9-D parameter space including the parameter t_c after maximizing inner product (6) over φ_c , this metric is given by,

$$\gamma_{\alpha\beta} = \frac{1}{2} (\mathcal{J} [\psi_\alpha \psi_\beta] - \mathcal{J} [\psi_\alpha] \mathcal{J} [\psi_\beta]), \quad (12)$$

where, ψ_α denotes the derivative of the TaylorF2 phase with respect to φ_α such that $\psi_\alpha = \partial\Psi/\partial\varphi_\alpha$. The quantity \mathcal{J} is the moment functional of the noise curve [53, 63], and is defined as follows for a given function $a(x)$,

$$\mathcal{J}[a(x)] = \int_{x_L}^{x_H} \frac{a(x)x^{-7/3}}{S_n(xf_0)} dx \Big/ \int_{x_L}^{x_H} \frac{x^{-7/3}}{S_n(xf_0)} dx \quad (13)$$

where $x_L = f_{\text{low}}/f_0$ and $x_H = f_{\text{high}}/f_0$ correspond to lowest and highest cutoff frequencies, respectively. The metric g_{ij} on the 8-D subspace, composed of PN-phasing coefficients, is obtained by projecting out the coalescence time t_c ,

$$g_{ij} = \gamma_{ij} - \frac{\gamma_{0i}\gamma_{0j}}{\gamma_{00}} \quad (14)$$

This projection operation corresponds to the minimization of the distance $\gamma_{\alpha\beta}\Delta\varphi^\alpha\Delta\varphi^\beta$ with respect to Δt_c [66]. Since the metric g_{ij} in 8-D parameter space has no dependence on the parameters (φ_i) itself. Therefore, the parameter space is globally flat in terms of these PN-phasing coefficients.

B. Effective dimensionality of the Parameter Space

The eigenvalues of g_{ij} are rapidly decreasing. In particular, the first two eigenvalues are significantly larger than the remaining ones. That indicates the effective dimension of the parameter space must be lower than the dimension of g_{ij} . The extent of the physically relevant region along many directions in the parameter space must be thinner than the maximum mismatch and therefore, we do not need to place templates in those regions of parameter space.

To identify the effective dimensionality of our parameter space composed of non-GR deviation parameters, we use the principal component analysis-based method proposed in [49]. We first transform to a Cartesian coordinate system by performing rotation and scaling so that the metric becomes the identity matrix. As a result, further rotations will leave the metric unchanged. As g_{ij} is a real-symmetric matrix, its eigenvectors form an orthonormal basis in \mathbb{R}^8 . The transformation produces a standard basis given by,

$$\tilde{\mu}_i = \sum_j \mathcal{R}_{ij} \mathcal{S}_{jj} \tilde{\varphi}_j, \quad (15)$$

where \mathcal{R} is a rotation matrix such that component \mathcal{R}_{ij} is the j^{th} element of the i^{th} eigenvector, and \mathcal{S} is a diagonal scaling matrix, the elements of which are square roots of eigenvalues.

The metric is an identity matrix in this new coordinate system, so we can place the templates using the most optimal \mathcal{A}_n^* lattice. The width of the parameter space is very thin along many directions, and placing templates in 8-D parameter space would be sub-optimal. Therefore, we perform Principle Component Analysis (PCA) to determine the effective dimension. First, we estimate the covariance matrix in $\tilde{\mu}_i$ coordinate system by generating a large number of points drawn from uniform distribution within the range of physical parameters as listed in Table I, and map them to $\tilde{\mu}_i$ coordinates using (15). Subsequently, we use eigenvectors of the covariance matrix to transform from $\tilde{\mu}_i$ to principal coordinates given by,

$$\xi_i = \sum_j C_{ij} \tilde{\mu}_j, \quad (16)$$

where C_{ij} is the j^{th} element of the i^{th} eigenvector. PCA assures that maximum parameter space extent would lie along ξ_1 direction and least along ξ_8 direction.

Figure 3 illustrates the extent of parameter space in ξ_i coordinates by depicting a large number of random points drawn from the uniform distribution of the physical parameters listed in Table I. The figure classifies two cases: the left column shows the extent of GR parameter space where all deviation parameters are set to zero, and the right column refers to the non-GR parameter space that allows deviation parameters to be non-zero. We opt to scale each ξ_i direction such that one unit refers to the coverage diameter of a template, $\mathcal{D}_{\text{max}} = 2\sqrt{1-MM}$, where MM stands for minimal match (0.97). This choice is made to visually identify the effective dimensions for placing the templates. For GR parameter space, one can easily notice that the extent along ξ_3 and ξ_4 directions is smaller than \mathcal{D}_{max} , while the directions ξ_1 and ξ_2 carry most of the parameter space extent, so a 2-D hexagonal lattice (\mathcal{A}_2^*) would be adequate to construct the template bank. On the other hand, for non-GR parameter space, the extent along the ξ_3 is almost twice of \mathcal{D}_{max} , and the extent along ξ_4 is five times smaller than \mathcal{D}_{max} . Therefore, we can place \mathcal{A}_3^* lattice in $\xi_1 - \xi_2 - \xi_3$ coordinates to cover the non-GR search space.

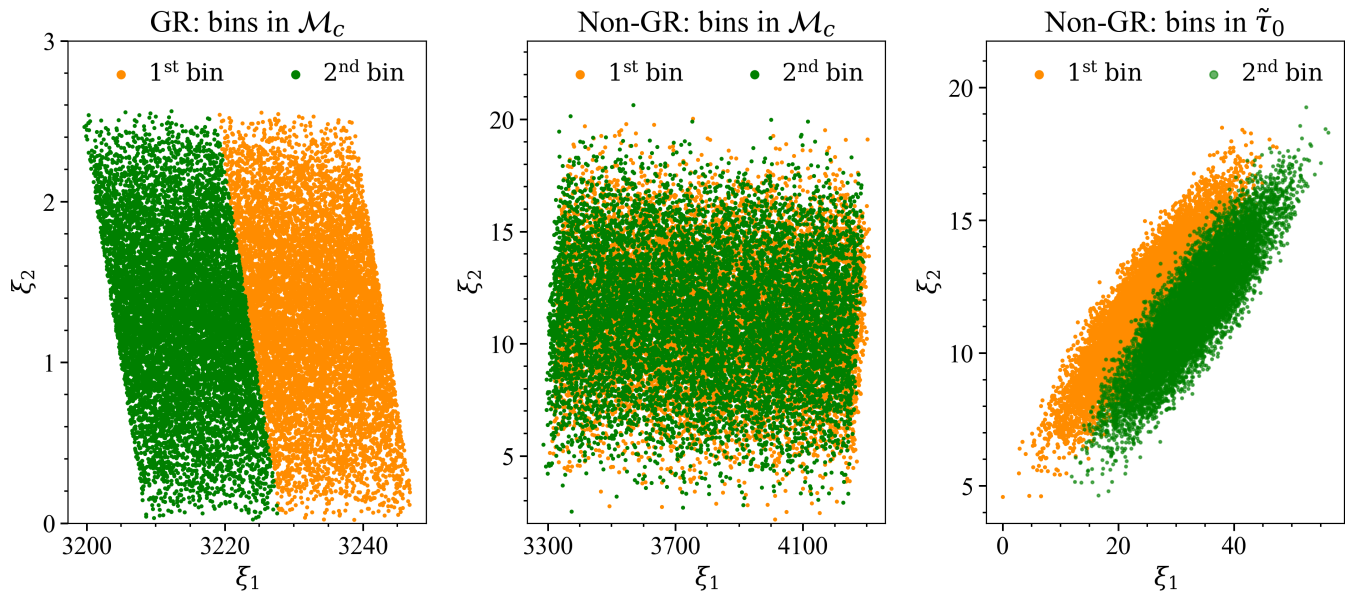


FIG. 4. An illustration of two consecutive bins over two most leading coordinates (ξ_1, ξ_2) , which is used to map the lattice points from ξ coordinate to physical parameter space. The left and middle panel shows the partitioning in chirp mass (\mathcal{M}_c) for GR and non-GR space, respectively. The chirp mass binning for non-GR parameter space fails to partition the parameter space due to the strong correlation between \mathcal{M}_c and 0PN deviation term ($\delta\hat{\varphi}_0$). We propose to use the 0PN chirp time ($\tilde{\tau}_0$) as shown in the right panel to partition the non-GR parameter space in ξ coordinates.

Although we can easily place the templates in ξ_i coordinates using \mathcal{A}_n^* lattice, but inverse mapping from ξ_i coordinates to physical parameters has yet to be discovered. On top of it, for the non-GR case we do not know the parameter space boundaries in ξ_i coordinates, which leads to an additional challenge to construct non-GR template bank.

C. Finding the lattice points in search parameter space

The GR search space is 4-D, comprising of component masses and spins. The non-GR search space is 12-D due to additional deviation parameters. The template points are generated in ξ coordinates, but there is no inverse mapping to obtain corresponding coordinates in physical search parameter space. Therefore, we follow a brute force method as carried out in previous studies [49, 65]. For a given lattice point, this method generates random points in the search parameter space and calculates their distance with the lattice point in ξ space. A random point is considered to be a solution when the distance is less than a pre-defined tolerance distance (`tol`). Throughout this work, we consider `tol` to be 10^{-2} , corresponding to a mismatch of 10^{-4} as given in Equation (9). The volume of a sphere with radius `tol` compared to the parameter space volume is $\mathcal{O}(10^6)$ and $\mathcal{O}(10^9)$ times smaller for GR and non-GR cases, respectively. Consequently, finding the solution for all lattice points would be computationally challenging. We allevi-

ate this issue by splitting out the parameter space into non-overlapping subspaces, and using the binary search algorithm KD Tree as implemented in SciPY [67] to find the nearest random point. The conventional partitioning scheme divides the parameter space over the chirp mass. The left panel of Figure 4 shows two consecutive bins over chirp mass ($\mathcal{M}_c = (m_1 m_2)^{3/5} / (m_1 + m_2)^{1/5}$) for GR parameter space, which are nearly non-overlapping. While for the non-GR case as shown in the middle panel, the two consecutive chirp mass bins are almost entirely overlapping—it's because of the strong degeneracy between chirp mass and 0PN deviation parameter $\delta\hat{\varphi}_0$. Here, we propose to use the 0PN chirp time ($\tilde{\tau}_0$) that depends on $\delta\hat{\varphi}_0$,

$$\tilde{\tau}_0 = \frac{5}{256} \mathcal{M}_c^{-5/3} (\pi f_0)^{-8/3} (1 + \delta\hat{\varphi}_0) \quad (17)$$

to partition the parameter space in ξ coordinates. The right panel of Figure 4 shows that $\tilde{\tau}_0$ binning reduces the overlap, but it's less efficient than chirp mass binning for GR space.

We choose those lattice points for which at least one random point is found within `tol` to construct a geometric template bank. This bank can cover the bulk region of the parameter space, but the boundaries would not be covered adequately. We use the top-down part of the hybrid geometric-random template placement method [50, 68, 69] by seeding the precomputed geometric bank. It starts by generating a large number of random points and then removes the points that are located

within the distance of $\mathcal{D}_{max}/2$ from the existing templates. Later, it picks one point arbitrarily from the remaining random points as a new template and removes those random points that lie at a distance $\leq \mathcal{D}_{max}/2$ from the chosen point. Continuing this process until all the random points get exhausted generates the hybrid bank.

Figure 3 shows the random points that are generated assuming uniform distribution over the parameters listed in Table I, where fewer random points lie near the boundaries. This is more prominent for non-GR case compared to GR. It happens even if we generate points inside a small bin, as shown in Figure 4. On the other hand, the boundaries of the non-GR parameter space are unknown and one can cover the boundary region by generating considerably larger number of random points, but that would be computationally challenging. A sub-optimal solution is to generate the random points assuming a uniform distribution in non-GR chirp time coordinates $(\tilde{\tau}_0, \tilde{\tau}_3)$, where $\tilde{\tau}_3$ corresponds to the non-spinning part of the 1.5PN term,

$$\tilde{\tau}_3 = \frac{1}{8\eta f_0} (\pi M f_0)^{-2/3} (1 + \delta\hat{\varphi}_3), \quad (18)$$

where M denotes the total mass of the binary ($M = m_1 + m_2$).

For construction of GR bank, we utilise the known boundaries in $\xi_1 - \xi_2$ plane and generate points using stochastic method along the boundaries. We generate 500 bins over \mathcal{M}_c as described above and simultaneously search for nearest random point for all the lattice as well as the boundary points in each bin on different CPU cores. We find that the (hybrid) GR bank contains 21,766 templates, out of which 15,447 corresponds to the \mathcal{A}_2^* star lattice (geometric GR bank) and rest corresponds to the boundaries. For construction of geometric non-GR bank we generate 1500 bins over $\tilde{\tau}_0$ as described above and search for nearest solution for lattice points in each bin independently on different CPU cores. This bank contains 284,467 templates. Subsequently, in order to provide coverage near boundary region, we initialize the top-down part of hybrid random template placement strategy with 200 million random proposals. 84,067 proposals get accepted as new templates resulting in a hybrid non-GR bank with 368,534 templates.

D. Failure of metric approximation – inclusion of exact match

While calculating the over-coverage of the non-GR hybrid bank (see Section IV), we inspected the distribution of match between closest pair of templates. More than 22% of templates are found to have the closest point with a match larger than the considered minimal match, as shown in Figure 7. It indicates a non-trivial over-coverage in the bank.

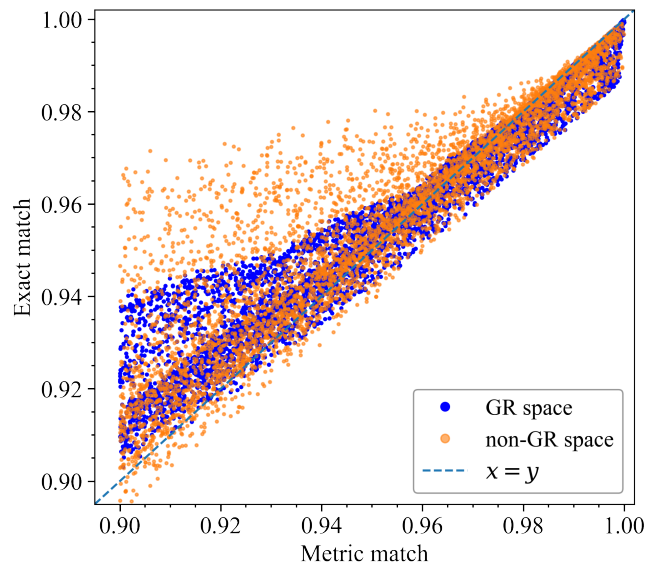


FIG. 5. A comparison between the match calculated using metric approximation as given by Equation (9) and the exact match as given by Equation (7), shown for two distinct cases: GR (blue dots) and non-GR (orange dots).

To comprehend the issue of over-coverage, we spray a large number of points in our parameter space, calculate the maximal match of each point with rest of the points using metric (approximate) match and exact match function as given in Equation (9) and (7), respectively. Figure 5 shows the comparison of metric match and the exact match for both GR and non-GR search spaces. For GR search space, we used \mathcal{A}_2^* lattice to place the templates, where the match between the two closest templates (inter-template match) is expected to be 0.91, but the exact match roughly varies between 0.91 and 0.94. The hybrid method would mostly place the templates near the boundaries, where the inter-template match can reach up to 0.97, and the corresponding exact match varies between 0.96 and 0.975. Consequently, the GR template bank can have over-coverage but not considerable. Similarly, for the non-GR search space, we used \mathcal{A}_3^* lattice (truncated octahedron) having two kinds of neighbors, one corresponding to square face and other corresponding to hexagonal face (see Appendix B of [50]). The inter-template match values for square and hexagonal faced neighbors are 0.904 and 0.928, respectively. Figure 5 suggests that although corresponding exact match varies across a wide range of values for the two inter-template metric match values, but only a mild fraction of points can have exact match above the minimal match (0.97). However, templates added using hybrid method can have (metric) match values as large as 0.97, where corresponding exact match can even be larger than 0.98 resulting in the observed over-coverage of hybrid non-GR bank. The large disagreement of the metric and exact match while incorporating the deviation parameters indicates the breakdown of metric approximation.

Bank	Type of match computation	Bank size	% of $\mathcal{FF} < 0.97$		Lowest \mathcal{FF}		Redundancy test % of $\mathcal{RF} > 0.97$
			GR	non-GR	GR	non-GR	
Geometric GR	metric	15 447	1.73	–	0.948	–	–
Hybrid GR	metric	21 766	1.26	100	0.962	–	3.9
Geometric non-GR	metric	284 467	–	0.52	–	0.917	0.0
Hybrid non-GR	metric	368 534	–	0.17	–	0.95	22.5
Hybrid non-GR	exact	337 352	–	0.26	–	0.959	0.0

TABLE II. Summary of the GR and Non-GR template banks that are constructed for BNS systems assuming the parameter ranges tabulated in Table I using TaylorF2 waveform with O2 PSD, and the lower cut-off frequency is set to be 27 Hz. The 4th and 5th columns report the results from bank validity—how much percentage of the injections are found with a fitting factor (\mathcal{FF}) below the desired minimal match value of 0.97. The GR bank is highly ineffectual in recovering non-GR signals as none of the injections is recovered above 0.97.

A recent study [70] described a similar breakdown of Fisher matrix approximation for constructing a template bank for BNS systems with tidal deformability. This study demonstrated that including higher-order terms in the Taylor series expansion of the match function can reliably compute the match. However, it is computationally more expensive than the brute-force computation of the exact match and therefore, can not be used in geometric placement. Following [68], we use the exact match function as given in Equation (7) only in the hybrid part of the template placement.

We generate 500 million proposals distributed uniformly in chirp-time coordinates $\{\tilde{\tau}_0, \tilde{\tau}_3\}$, component spins $\{\chi_{1z}, \chi_{2z}\}$ and deviation parameters $\{\delta\hat{\varphi}_i\}$ within their respective limits as given in Table I and use minimal match criteria to be 0.965 while constructing hybrid non-GR bank. 52,885 proposals get accepted as new templates. The inclusion of exact match and slightly relaxing the minimal match criteria, resolves the redundancy issue with 8.5% reduction in bank size. We summarize the size of the geometric and hybrid template banks in Table II.

It takes $\sim 11,500$ CPU hours to construct geometric non-GR bank. Generation of the hybrid bank, using geometric bank as the seed, takes ~ 3500 CPU hours.

IV. TEMPLATE BANK VALIDITY AND REDUNDANCY

To quantify the performance of the template banks, we carry out Monte Carlo simulations to calculate the distribution of the fitting factor for a large set of injections. The fitting factor value for a waveform tells us what fraction of SNR can be recovered, and the distribution can identify the regions of parameter space where the bank coverage is poor. We generate 10^5 signals using the TaylorF2 waveform model. The intrinsic parameters are drawn from a uniform distribution within their respective boundaries listed in Table I. The fitting factors for non-precessing binary systems are independent of the extrinsic parameters: the sky location, polarization angle and inclination angles. That criteria also holds for

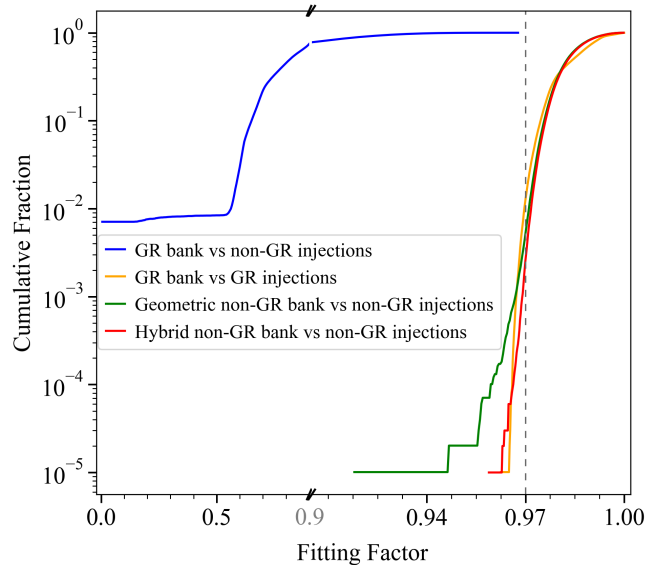


FIG. 6. Effectualness of the template banks for a set of 10^5 TaylorF2 injections generated randomly within their target search spaces described in Table I. We note that for the geometric non-GR bank, although only 0.52% of injections are recovered with a fitting factor below the minimal match of the bank (0.97), but it drops to 0.917 for the worst fitting injection. The complete description of the performance of the banks is listed in Table II. Note that the broken x-axis (splitted at 0.9) is used to accommodate all the Fitting factor distributions together.

non-GR signals. While calculating the fitting factor using Equation (8), we generate both the template and injection waveforms with a fixed lower cutoff frequency of 27 Hz.

Figure 1 shows the fitting factor distribution of the GR template bank for recovering the non-GR signals. Earlier, we noted that *all* the injections are recovered below the fitting factor of 0.97, which implies that the GR template bank is highly ineffectual for detecting the non-GR signals. Whereas our new hybrid non-GR template bank has recovered *almost all* the injections above a fitting

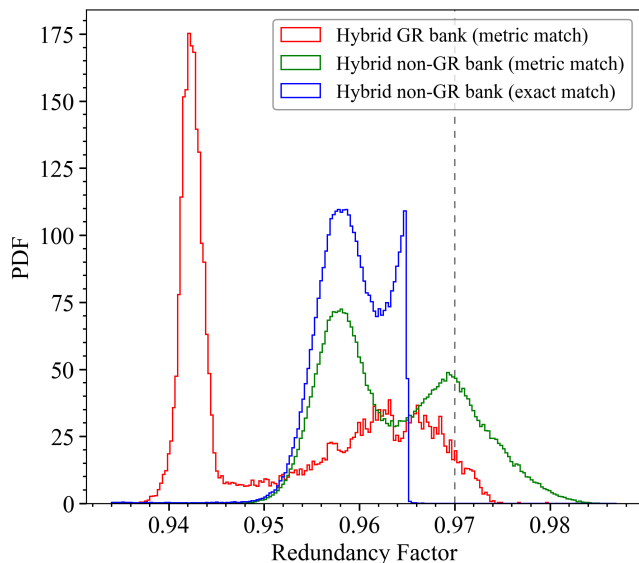


FIG. 7. Redundancy test of GR as well as non-GR banks. Here, the redundancy factor is calculated for every template against the rest of the templates in the bank. The hybrid non-GR bank with metric match indicates a significant overcoverage, where 22.5% templates are found above the minimal match of the bank (0.97). The complete description of the redundancy test of the banks is listed in Table II.

factor of 0.97, as shown in Figure 6. We summarize the fitting factor results in Table II.

We perform the redundancy test of a template bank by calculating the maximal match between a targeted template waveform (h_i) and every template waveform (h_j) in the bank excluding the template in question [71], we call it the redundancy factor (\mathcal{RF}),

$$\mathcal{RF}(h_i) = \max_{1 \leq j \leq n_T, j \neq i} \mathcal{M}(h_i, h_j), \quad (19)$$

where n_T is the number of templates in the bank. Ideally, the redundancy factor for any template should not be larger than the minimal match used to construct the bank. Figure 7 shows the distribution of the redundancy factor for different template banks. For the hybrid non-GR bank constructed using metric match, 22.5% of templates have a redundancy factor larger than 0.97, which indicates a significant overcoverage. For comparison, we also construct a similar plot for GR bank and find that for this case, only 3.9% of the templates have the redundancy factor larger than 0.97.

V. DISCUSSION AND CONCLUSION

In this work, we have investigated the performance of a GR-template bank for searching the non-GR signals from BNS systems where component masses range from 1 to 2.4 M_\odot , and the phenomenological deviation parameters span 1σ width of the posterior distribution

measured from GW170817 event. With the LIGO’s O2 sensitivity, we have noticed that most of the non-GR signals could be missed by the GR template bank. We have presented a hybrid method for constructing a template bank for searches of beyond GR signals. We have found that our non-GR bank size is ~ 15 times larger than the conventional GR bank. We have shown that our new bank is faithful in detecting the non-GR signals in its target search space, whereas the GR bank could not recover any non-GR signal above a fitting factor value of 0.97.

The previous study exploring the searches of non-GR signals [1] targeted the search space relevant for BBH systems, and the parametrized deviations were considered in the lower PN terms and constructed an 8-D template bank using the straightforward stochastic method. In this work, we target the 12-D search space of BNS systems, including the deviation in all the PN terms up to 3.5PN, and present a hybrid method by combining the space efficiency of the geometric method and the robustness of the random method. In this work, we restrict ourselves to use only the fractional deviations i.e., the deviation over the non-zero PN coefficients. In theory one can include deviations on the PN terms for which the coefficient value is zero in GR. This method can be used wherever the TaylorF2 waveform model is applicable, such as searches of subsolar mass (SSM) compact binary, including eccentricity for SSM/BNS and searches of stellar mass binaries with space-based detectors [71].

In future work, we intend to conduct searches of non-GR signals from BNS-like mergers with the LIGO and Virgo’s data during the first and second observation runs. A single detection of this type of source could reveal a novel formation channel for compact binaries.

VI. ACKNOWLEDGEMENTS

We thank Ian Harry for carefully reading the manuscript and for offering several comments and suggestions to improve the presentation and content of the paper. We are highly grateful for the suggestions received from Alex Nielsen, Tito Dal Canton and Thomas Dent. A.S. thanks IIT Gandhinagar for the research fellowship. S.R. was supported by the research program of the Netherlands Organization for Scientific Research (NWO). We acknowledge computational resources provided by IIT Gandhinagar and also thank HPC support staff at IIT Gandhinagar for their help and cooperation. We gratefully acknowledge computational resources provided by the LIGO Laboratory and supported by the NSF Grants No. PHY-0757058 and No. PHY-0823459. This research has made use of data, software and/or web tools obtained from the Gravitational Wave Open Science Center, a service of LIGO Laboratory [72], the LIGO Scientific Collaboration and the Virgo Collaboration. The material of this paper is based upon work supported by NSF’s LIGO Laboratory, which is a major facility fully

funded by the National Science Foundation (NSF). This document has LIGO DCC No. LIGO-P2300373.

and Matplotlib [76].

Appendix A: PN coefficients

Softwares. To obtain the waveforms and PN coefficients, we use the LALSIMULATION package of the LIGO Algorithms Library (LAL) software suite [73]. The fitting factors studies were performed by modifying `pycbc_banksim` code implemented in the `PyCBC` library [74]. Our analysis utilize Numpy [75], Scipy [67]

Here, we describe the PN expansion coefficients of TaylorF2 waveform phase as mentioned in Equation (2). The waveform phase contains corrections to Newtonian order up to 3.5PN order in non-spinning and linear spin-orbit effects [77, 78] and up to 3PN order in quadratic spin effects [79].

$$\varphi_0 = \frac{3}{128\eta} (\pi M f_0)^{-5/3} \quad (\text{A1a})$$

$$\varphi_2 = \frac{3}{128\eta} \left(\frac{3715}{756} + \frac{55\eta}{9} \right) (\pi M f_0)^{-1} \quad (\text{A1b})$$

$$\varphi_3 = \frac{3}{128\eta} \left\{ -16\pi + \frac{113\delta\chi_a}{3} + \left(\frac{113}{3} - \frac{76\eta}{3} \right) \chi_s \right\} (\pi M f_0)^{-2/3} \quad (\text{A1c})$$

$$\begin{aligned} \varphi_4 = \frac{3}{128\eta} \left\{ \frac{15293365}{508032} + \frac{27145\eta}{504} + \frac{3085\eta^2}{72} + \left(-\frac{405}{8} + 200\eta \right) \chi_a^2 - \frac{405}{4} \delta\chi_a\chi_s \right. \\ \left. + \left(-\frac{405}{8} + \frac{5\eta}{2} \right) \chi_s^2 \right\} (\pi M f_0)^{-1/3} \end{aligned} \quad (\text{A1d})$$

$$\varphi_5^\ell = \frac{3}{128\eta} \left\{ \frac{38645\pi}{756} - \frac{65\pi\eta}{9} + \delta \left(-\frac{732985}{2268} - \frac{140\eta}{9} \right) \chi_a + \left(-\frac{732985}{2268} + \frac{24260\eta}{81} + \frac{340\eta^2}{9} \right) \chi_s \right\} \log(\pi M f_0) \quad (\text{A1e})$$

$$\begin{aligned} \varphi_6 = \frac{3}{128\eta} \left\{ \frac{11583231236531}{4694215680} - \frac{6848\gamma_E}{21} - \frac{640\pi^2}{3} + \left(-\frac{15737765635}{3048192} + \frac{2255\pi^2}{12} \right) \eta + \frac{76055\eta^2}{1728} - \frac{127825\eta^3}{1296} \right. \\ \left. - \frac{6848}{63} \log 64 + \frac{2270}{3} \pi\delta\chi_a + \left(\frac{2270\pi}{3} - 520\pi\eta \right) \chi_s + \left(\frac{75515}{144} \delta - \frac{8225}{18} \delta\eta \right) \chi_s\chi_a \right. \\ \left. + \left(-480\eta^2 - \frac{263245}{252} \eta + \frac{75515}{288} \right) \chi_a^2 + \left(\frac{1255}{9} \eta^2 - \frac{232415}{504} \eta + \frac{75515}{288} \right) \chi_s^2 \right\} (\pi M f_0)^{1/3} \end{aligned} \quad (\text{A1f})$$

$$\varphi_6^\ell = -\frac{107}{42\eta} \log(\pi M f_0) (\pi M f_0)^{1/3} \quad (\text{A1g})$$

$$\begin{aligned} \varphi_7 = \frac{3}{128\eta} \left\{ \frac{77096675\pi}{254016} + \frac{378515\pi\eta}{1512} - \frac{74045\pi\eta^2}{756} + \delta \left(-\frac{25150083775}{3048192} + \frac{26804935\eta}{6048} - \frac{1985\eta^2}{48} \right) \chi_a \right. \\ \left. + \left(-\frac{25150083775}{3048192} + \frac{10566655595\eta}{762048} - \frac{1042165\eta^2}{3024} + \frac{5345\eta^3}{36} \right) \chi_s \right\} (\pi M f_0)^{2/3} \end{aligned} \quad (\text{A1h})$$

where $\gamma_E \approx 0.577216$ is the Euler constant, $M \equiv m_1 + m_2$ is the total mass of the binary, $\eta \equiv m_1 m_2 / M^2$ is

symmetric mass ratio, $\delta \equiv (m_1 - m_2) / M$ is asymmetric mass ratio, $\chi_s \equiv (\chi_1 + \chi_2) / 2$ and $\chi_a \equiv (\chi_1 - \chi_2) / 2$ are symmetric and asymmetric combination of the spins.

[1] H. Narola, S. Roy, and A. S. Sengupta, Beyond general relativity: Designing a template-based search for exotic gravitational wave signals, *Phys. Rev. D* **107**, 024017 (2023), arXiv:2207.10410 [gr-qc].

[2] J. Aasi *et al.* (LIGO Scientific), Advanced LIGO, *Class.*

Quant. Grav. **32**, 074001 (2015), arXiv:1411.4547 [gr-qc].

[3] F. Acernese *et al.* (VIRGO), Advanced Virgo: a second-generation interferometric gravitational wave detector, *Class. Quant. Grav.* **32**, 024001 (2015), arXiv:1408.3978 [gr-qc].

- [4] Y. Aso, Y. Michimura, K. Somiya, M. Ando, O. Miyakawa, T. Sekiguchi, D. Tatsumi, and H. Yamamoto (KAGRA), Interferometer design of the KAGRA gravitational wave detector, *Phys. Rev. D* **88**, 043007 (2013), [arXiv:1306.6747 \[gr-qc\]](#).
- [5] B. P. Abbott *et al.* (LIGO Scientific, Virgo), GWTC-1: A Gravitational-Wave Transient Catalog of Compact Binary Mergers Observed by LIGO and Virgo during the First and Second Observing Runs, *Phys. Rev. X* **9**, 031040 (2019), [arXiv:1811.12907 \[astro-ph.HE\]](#).
- [6] R. Abbott *et al.* (LIGO Scientific, Virgo), GWTC-2: Compact Binary Coalescences Observed by LIGO and Virgo During the First Half of the Third Observing Run, *Phys. Rev. X* **11**, 021053 (2021), [arXiv:2010.14527 \[gr-qc\]](#).
- [7] R. Abbott *et al.* (LIGO Scientific, VIRGO, KAGRA), GWTC-3: Compact Binary Coalescences Observed by LIGO and Virgo During the Second Part of the Third Observing Run, [arXiv e-prints](#), [arXiv:2111.03606 \(2021\)](#), [arXiv:2111.03606 \[gr-qc\]](#).
- [8] B. P. Abbott *et al.* (LIGO Scientific, Virgo), Tests of general relativity with GW150914, *Phys. Rev. Lett.* **116**, 221101 (2016), [Erratum: *Phys. Rev. Lett.* **121**, 129902 (2018)], [arXiv:1602.03841 \[gr-qc\]](#).
- [9] B. P. Abbott *et al.* (LIGO Scientific, Virgo), Tests of General Relativity with GW170817, *Phys. Rev. Lett.* **123**, 011102 (2019), [arXiv:1811.00364 \[gr-qc\]](#).
- [10] B. P. Abbott *et al.* (LIGO Scientific, Virgo), Tests of General Relativity with the Binary Black Hole Signals from the LIGO-Virgo Catalog GWTC-1, *Phys. Rev. D* **100**, 104036 (2019), [arXiv:1903.04467 \[gr-qc\]](#).
- [11] R. Abbott *et al.* (LIGO Scientific, Virgo), Tests of general relativity with binary black holes from the second LIGO-Virgo gravitational-wave transient catalog, *Phys. Rev. D* **103**, 122002 (2021), [arXiv:2010.14529 \[gr-qc\]](#).
- [12] R. Abbott *et al.* (LIGO Scientific, VIRGO, KAGRA), Tests of General Relativity with GWTC-3, [arXiv e-prints](#), [arXiv:2112.06861 \(2021\)](#), [arXiv:2112.06861 \[gr-qc\]](#).
- [13] C. M. Will, The Confrontation between General Relativity and Experiment, *Living Rev. Rel.* **17**, 4 (2014), [arXiv:1403.7377 \[gr-qc\]](#).
- [14] I. H. Stairs, Testing general relativity with pulsar timing, *Living Rev. Rel.* **6**, 5 (2003), [arXiv:astro-ph/0307536](#).
- [15] N. Wex, Testing Relativistic Gravity with Radio Pulsars, [arXiv e-prints](#), [arXiv:1402.5594 \(2014\)](#), [arXiv:1402.5594 \[gr-qc\]](#).
- [16] M. Kramer *et al.*, Strong-Field Gravity Tests with the Double Pulsar, *Phys. Rev. X* **11**, 041050 (2021), [arXiv:2112.06795 \[astro-ph.HE\]](#).
- [17] R. Abuter *et al.* (GRAVITY), Detection of the gravitational redshift in the orbit of the star S2 near the Galactic centre massive black hole, *Astron. Astrophys.* **615**, L15 (2018), [arXiv:1807.09409 \[astro-ph.GA\]](#).
- [18] T. Do *et al.*, Relativistic redshift of the star S0-2 orbiting the Galactic center supermassive black hole, *Science* **365**, 664 (2019), [arXiv:1907.10731 \[astro-ph.GA\]](#).
- [19] K. Akiyama *et al.* (Event Horizon Telescope), First M87 Event Horizon Telescope Results. IV. Imaging the Central Supermassive Black Hole, *Astrophys. J. Lett.* **875**, L4 (2019), [arXiv:1906.11241 \[astro-ph.GA\]](#).
- [20] M. Okounkova, L. C. Stein, M. A. Scheel, and D. A. Hemberger, Numerical binary black hole mergers in dynamical Chern-Simons gravity: Scalar field, *Phys. Rev. D* **96**, 044020 (2017), [arXiv:1705.07924 \[gr-qc\]](#).
- [21] M. Okounkova, L. C. Stein, J. Moxon, M. A. Scheel, and S. A. Teukolsky, Numerical relativity simulation of GW150914 beyond general relativity, *Phys. Rev. D* **101**, 104016 (2020), [arXiv:1911.02588 \[gr-qc\]](#).
- [22] M. Okounkova, Numerical relativity simulation of GW150914 in Einstein dilaton Gauss-Bonnet gravity, *Phys. Rev. D* **102**, 084046 (2020), [arXiv:2001.03571 \[gr-qc\]](#).
- [23] R. N. Lang, Compact binary systems in scalar-tensor gravity. III. Scalar waves and energy flux, *Phys. Rev. D* **91**, 084027 (2015), [arXiv:1411.3073 \[gr-qc\]](#).
- [24] N. Sennett, S. Marsat, and A. Buonanno, Gravitational waveforms in scalar-tensor gravity at 2PN relative order, *Phys. Rev. D* **94**, 084003 (2016), [arXiv:1607.01420 \[gr-qc\]](#).
- [25] L. Bernard, Dynamics of compact binary systems in scalar-tensor theories: II. Center-of-mass and conserved quantities to 3PN order, *Phys. Rev. D* **99**, 044047 (2019), [arXiv:1812.04169 \[gr-qc\]](#).
- [26] N. Sennett, R. Brito, A. Buonanno, V. Gorbenko, and L. Senatore, Gravitational-Wave Constraints on an Effective Field-Theory Extension of General Relativity, *Phys. Rev. D* **102**, 044056 (2020), [arXiv:1912.09917 \[gr-qc\]](#).
- [27] F.-L. Julié and E. Berti, Post-Newtonian dynamics and black hole thermodynamics in Einstein-scalar-Gauss-Bonnet gravity, *Phys. Rev. D* **100**, 104061 (2019), [arXiv:1909.05258 \[gr-qc\]](#).
- [28] N. J. Cornish and T. B. Littenberg, BayesWave: Bayesian Inference for Gravitational Wave Bursts and Instrument Glitches, *Class. Quant. Grav.* **32**, 135012 (2015), [arXiv:1410.3835 \[gr-qc\]](#).
- [29] S. Ghonge, K. Chatziioannou, J. A. Clark, T. Littenberg, M. Millhouse, L. Cadonati, and N. Cornish, Reconstructing gravitational wave signals from binary black hole mergers with minimal assumptions, *Phys. Rev. D* **102**, 064056 (2020), [arXiv:2003.09456 \[gr-qc\]](#).
- [30] S. Roy, Nonorthogonal wavelet transformation for reconstructing gravitational wave signals, *Phys. Rev. Res.* **4**, 033078 (2022), [arXiv:2201.01526 \[gr-qc\]](#).
- [31] A. Ghosh *et al.*, Testing general relativity using golden black-hole binaries, *Phys. Rev. D* **94**, 021101 (2016), [arXiv:1602.02453 \[gr-qc\]](#).
- [32] A. Maselli, P. Pani, L. Gualtieri, and E. Berti, Parametrized ringdown spin expansion coefficients: a data-analysis framework for black-hole spectroscopy with multiple events, *Phys. Rev. D* **101**, 024043 (2020), [arXiv:1910.12893 \[gr-qc\]](#).
- [33] M. Agathos, W. Del Pozzo, T. G. F. Li, C. Van Den Broeck, J. Veitch, and S. Vitale, TIGER: A data analysis pipeline for testing the strong-field dynamics of general relativity with gravitational wave signals from coalescing compact binaries, *Phys. Rev. D* **89**, 082001 (2014), [arXiv:1311.0420 \[gr-qc\]](#).
- [34] J. Meidam, M. Agathos, C. Van Den Broeck, J. Veitch, and B. S. Sathyaprakash, Testing the no-hair theorem with black hole ringdowns using TIGER, *Phys. Rev. D* **90**, 064009 (2014), [arXiv:1406.3201 \[gr-qc\]](#).
- [35] A. K. Mehta, A. Buonanno, R. Cotesta, A. Ghosh, N. Sennett, and J. Steinhoff, Tests of general relativity with gravitational-wave observations using a flexible theory-independent method, *Phys. Rev. D* **107**, 044020 (2023), [arXiv:2203.13937 \[gr-qc\]](#).
- [36] M. Saleem, S. Datta, K. G. Arun, and B. S. Sathyaprakash, Parametrized tests of post-Newtonian

- theory using principal component analysis, *Phys. Rev. D* **105**, 084062 (2022), arXiv:2110.10147 [gr-qc].
- [37] S. Klimentko, I. Yakushin, A. Mercer, and G. Mitsel-makher, Coherent method for detection of gravitational wave bursts, *Class. Quant. Grav.* **25**, 114029 (2008), arXiv:0802.3232 [gr-qc].
- [38] M. Drago, S. Klimentko, C. Lazzaro, E. Milotti, G. Mitsel-makher, V. Necula, B. O'Brian, G. A. Prodi, F. Salemi, M. Szczepanczyk, S. Tiwari, V. Tiwari, V. Gayathri, G. Vedovato, and I. Yakushin, coherent WaveBurst, a pipeline for unmodeled gravitational-wave data analysis, *SoftwareX* **14**, 100678 (2021), arXiv:2006.12604 [gr-qc].
- [39] R. Lynch, S. Vitale, R. Essick, E. Katsavounidis, and F. Robinet, Information-theoretic approach to the gravitational-wave burst detection problem, *Phys. Rev. D* **95**, 104046 (2017), arXiv:1511.05955 [gr-qc].
- [40] F. Robinet, N. Arnaud, N. Leroy, A. Lundgren, D. Macleod, and J. McIver, Omicron: A tool to characterize transient noise in gravitational-wave detectors, *SoftwareX* **12**, 100620 (2020), arXiv:2007.11374 [astro-ph.IM].
- [41] C. Messick, K. Blackburn, P. Brady, P. Brockill, K. Cannon, R. Cariou, S. Caudill, S. J. Chamberlin, J. D. E. Creighton, R. Everett, C. Hanna, D. Keppel, R. N. Lang, T. G. F. Li, D. Meacher, A. Nielsen, C. Pankow, S. Privitera, H. Qi, S. Sachdev, L. Sadeghian, L. Singer, E. G. Thomas, L. Wade, M. Wade, A. Weinstein, and K. Wiesner, Analysis framework for the prompt discovery of compact binary mergers in gravitational-wave data, *Phys. Rev. D* **95**, 042001 (2017), arXiv:1604.04324 [astro-ph.IM].
- [42] L. Tsukada *et al.*, Improved ranking statistics of the GstLAL inspiral search for compact binary coalescences, *Phys. Rev. D* **108**, 043004 (2023), arXiv:2305.06286 [astro-ph.IM].
- [43] F. Aubin *et al.*, The MBTA pipeline for detecting compact binary coalescences in the third LIGO–Virgo observing run, *Class. Quant. Grav.* **38**, 095004 (2021), arXiv:2012.11512 [gr-qc].
- [44] S. A. Usman *et al.*, The PyCBC search for gravitational waves from compact binary coalescence, *Class. Quant. Grav.* **33**, 215004 (2016), arXiv:1508.02357 [gr-qc].
- [45] A. H. Nitz, T. Dal Canton, D. Davis, and S. Reyes, Rapid detection of gravitational waves from compact binary mergers with PyCBC Live, *Phys. Rev. D* **98**, 024050 (2018), arXiv:1805.11174 [gr-qc].
- [46] T. Dal Canton, A. H. Nitz, B. Gadre, G. S. Cabourn Davies, V. Villa-Ortega, T. Dent, I. Harry, and L. Xiao, Real-time Search for Compact Binary Mergers in Advanced LIGO and Virgo's Third Observing Run Using PyCBC Live, *Astrophys. J.* **923**, 254 (2021), arXiv:2008.07494 [astro-ph.HE].
- [47] Q. Chu *et al.*, SPIIR online coherent pipeline to search for gravitational waves from compact binary coalescences, *Phys. Rev. D* **105**, 024023 (2022), arXiv:2011.06787 [gr-qc].
- [48] A. A. Shoom, P. K. Gupta, B. Krishnan, A. B. Nielsen, and C. D. Capano, Testing the post-Newtonian expansion with GW170817, *General Relativity and Gravitation* **55**, 55 (2023), arXiv:2105.02191 [gr-qc].
- [49] D. A. Brown, I. Harry, A. Lundgren, and A. H. Nitz, Detecting binary neutron star systems with spin in advanced gravitational-wave detectors, *Phys. Rev. D* **86**, 084017 (2012), arXiv:1207.6406 [gr-qc].
- [50] S. Roy, A. S. Sengupta, and N. Thakor, Hybrid geometric-random template-placement algorithm for gravitational wave searches from compact binary coalescences, *Phys. Rev. D* **95**, 104045 (2017), arXiv:1702.06771 [gr-qc].
- [51] D. R. Lorimer and M. Kramer, *Handbook of Pulsar Astronomy*, Vol. 4 (2004).
- [52] L. Blanchet, Gravitational Radiation from Post-Newtonian Sources and Inspiralling Compact Binaries, *Living Rev. Rel.* **17**, 2 (2014), arXiv:1310.1528 [gr-qc].
- [53] E. Poisson and C. M. Will, Gravitational waves from inspiraling compact binaries: Parameter estimation using second postNewtonian wave forms, *Phys. Rev. D* **52**, 848 (1995), arXiv:gr-qc/9502040.
- [54] A. Buonanno, B. Iyer, E. Ochsner, Y. Pan, and B. S. Sathyaprakash, Comparison of post-Newtonian templates for compact binary inspiral signals in gravitational-wave detectors, *Phys. Rev. D* **80**, 084043 (2009), arXiv:0907.0700 [gr-qc].
- [55] C. K. Mishra, K. G. Arun, B. R. Iyer, and B. S. Sathyaprakash, Parametrized tests of post-Newtonian theory using Advanced LIGO and Einstein Telescope, *Phys. Rev. D* **82**, 064010 (2010), arXiv:1005.0304 [gr-qc].
- [56] T. G. F. Li, W. Del Pozzo, S. Vitale, C. Van Den Broeck, M. Agathos, J. Veitch, K. Grover, T. Sidery, R. Sturani, and A. Vecchio, Towards a generic test of the strong field dynamics of general relativity using compact binary coalescence, *Phys. Rev. D* **85**, 082003 (2012), arXiv:1110.0530 [gr-qc].
- [57] J. Meidam *et al.*, Parametrized tests of the strong-field dynamics of general relativity using gravitational wave signals from coalescing binary black holes: Fast likelihood calculations and sensitivity of the method, *Phys. Rev. D* **97**, 044033 (2018), arXiv:1712.08772 [gr-qc].
- [58] B. P. Abbott *et al.* (LIGO Scientific Collaboration and Virgo Collaboration), Tests of General Relativity with GW170817, *Phys. Rev. Lett.* **123**, 011102 (2019).
- [59] B. S. Sathyaprakash and S. V. Dhurandhar, Choice of filters for the detection of gravitational waves from coalescing binaries, *Phys. Rev. D* **44**, 3819 (1991).
- [60] S. V. Dhurandhar and B. S. Sathyaprakash, Choice of filters for the detection of gravitational waves from coalescing binaries. 2. Detection in colored noise, *Phys. Rev. D* **49**, 1707 (1994).
- [61] B. Allen, W. G. Anderson, P. R. Brady, D. A. Brown, and J. D. E. Creighton, FINDCHIRP: An Algorithm for detection of gravitational waves from inspiraling compact binaries, *Phys. Rev. D* **85**, 122006 (2012), arXiv:gr-qc/0509116.
- [62] T. A. Apostolatos, Search templates for gravitational waves from precessing, inspiraling binaries, *Phys. Rev. D* **52**, 605 (1995).
- [63] B. J. Owen, Search templates for gravitational waves from inspiraling binaries: Choice of template spacing, *Phys. Rev. D* **53**, 6749 (1996), arXiv:gr-qc/9511032.
- [64] B. J. Owen and B. S. Sathyaprakash, Matched filtering of gravitational waves from inspiraling compact binaries: Computational cost and template placement, *Phys. Rev. D* **60**, 022002 (1999), arXiv:gr-qc/9808076.
- [65] I. W. Harry, A. H. Nitz, D. A. Brown, A. P. Lundgren, E. Ochsner, and D. Keppel, Investigating the effect of precession on searches for neutron-star–black-hole binaries with advanced ligo, *Phys. Rev. D* **89**, 024010 (2014).
- [66] E. K. Porter, Computational resources to filter gravita-

- tional wave data with p-approximant templates, *Classical and Quantum Gravity* **19**, 4343 (2002).
- [67] P. Virtanen *et al.*, SciPy 1.0—Fundamental Algorithms for Scientific Computing in Python, *Nature Meth.* **17**, 261 (2020), [arXiv:1907.10121 \[cs.MS\]](#).
- [68] S. Roy, A. S. Sengupta, and P. Ajith, Effectual template banks for upcoming compact binary searches in Advanced-LIGO and Virgo data, *Phys. Rev. D* **99**, 024048 (2019), [arXiv:1711.08743 \[gr-qc\]](#).
- [69] S. Roy, A. Sankar Sengupta, and P. Ajith, Geometric-stochastic template banks for gravitational wave searches from compact binaries in advanced-LIGO data, in *42nd COSPAR Scientific Assembly*, Vol. 42 (2018) pp. E1.15–36–18.
- [70] I. Harry and A. Lundgren, Failure of the Fisher matrix when including tidal terms: Considering construction of template banks of tidally deformed binary neutron stars, *Phys. Rev. D* **104**, 043008 (2021), [arXiv:2101.01091 \[gr-qc\]](#).
- [71] H. Wang, I. Harry, A. Nitz, and Y.-M. Hu, The Challenge of Eccentricity when Observing Stellar-mass Binary Black Holes with Space-Based Gravitational Wave Detectors, [arXiv e-prints](#) , [arXiv:2304.10340 \(2023\)](#), [arXiv:2304.10340 \[astro-ph.HE\]](#).
- [72] M. Vallisneri, J. Kanner, R. Williams, A. Weinstein, and B. Stephens, The LIGO Open Science Center, *Journal of Physics: Conference Series* **610**, 012021 (2015).
- [73] LIGO Scientific Collaboration, *LIGO Algorithm Library - LALSuite*, free software (GPL) (2023).
- [74] A. Nitz, I. Harry, D. Brown, C. M. Biwer, J. Willis, T. D. Canton, C. Capano, T. Dent, L. Pekowsky, S. De, M. Cabero, G. S. C. Davies, A. R. Williamson, D. Macleod, B. Machenschalk, F. Pannarale, P. Kumar, S. Reyes, dfinstad, S. Kumar, M. Tápai, S. Wu, L. Singer, veronica villa, S. Khan, S. Fairhurst, K. Chandra, A. Nielsen, S. Singh, and T. Massinger, [gwastro/pycbc: v2.2.0 release of PyCBC](#) (2023).
- [75] C. R. Harris *et al.*, Array programming with NumPy, *Nature* **585**, 357 (2020), [arXiv:2006.10256 \[cs.MS\]](#).
- [76] J. D. Hunter, Matplotlib: A 2D Graphics Environment, *Comput. Sci. Eng.* **9**, 90 (2007).
- [77] K. G. Arun, A. Buonanno, G. Faye, and E. Ochsner, Higher-order spin effects in the amplitude and phase of gravitational waveforms emitted by inspiraling compact binaries: Ready-to-use gravitational waveforms, *Phys. Rev. D* **79**, 104023 (2009), [Erratum: *Phys.Rev.D* 84, 049901 (2011)], [arXiv:0810.5336 \[gr-qc\]](#).
- [78] A. Bohé, S. Marsat, and L. Blanchet, Next-to-next-to-leading order spin-orbit effects in the gravitational wave flux and orbital phasing of compact binaries, *Classical and Quantum Gravity* **30**, 135009 (2013), [arXiv:1303.7412 \[gr-qc\]](#).
- [79] A. Bohé, G. Faye, S. Marsat, and E. K. Porter, Quadratic-in-spin effects in the orbital dynamics and gravitational-wave energy flux of compact binaries at the 3PN order, *Classical and Quantum Gravity* **32**, 195010 (2015), [arXiv:1501.01529 \[gr-qc\]](#).